Phase Selectivity and Stability in Compositionally Complex Nano $(n\mathrm{A}_{1/n})\mathrm{Co}_2\mathrm{O}_4$

Xin Wang,[†] Peter Metz,[†] Eleonora Calì,[‡,§] Palani Raja Jothi,[†,‖] Eric Andrew Lass,[†] and Katharine Page[*,†,¶]

[†]*Department of Materials Science and Engineering, University of Tennessee, Knoxville, Tennessee 37996 USA.*

[‡]*Department of Materials, Imperial College London,Exhibition Road,London SW72AZ UK.*

[¶]*Neutron Scattering Division, Oak Ridge National Laboratory, Oak Ridge, Tennessee 37831 USA.*

[§]*Current address: Department of Applied Science and Technology, Politecnico di Torino, Turin 10129 Italy.*

[‖]*Current address: JTEC Energy Inc, Atlanta, Georgia 30312 USA.*

E-mail: kpage10@utk.edu

Abstract

A family of compositionally complex spinels with the formula of $(n\mathrm{A}_{1/n})\mathrm{Co}_2\mathrm{O}_4$ (A = combinations of Mg, Cr, Mn, Fe, Co, Ni, Cu, and Zn) was synthesized using a low-temperature soft-templating method. The phase selectivity and the temperature stability window for the series were found to depend strongly upon A-site composition and only modestly on the number of elements (n) present on the A site. Select control reactions and in situ high temperature X-ray diffraction (XRD) uncovered a propensity for temperature-activated de-mixing for compositions containing Mg, Ni, Mn, and Fe. The A-site cations exhibit spatially heterogeneous distributions in the *as-formed*

spinels, which diminishes with intermediate thermal annealing, as shown by scanning-transmission electron microscopy/energy dispersive spectroscopy (STEM/EDS) and X-ray line profile analysis. The single spinel phases obtained are metastable, separating into a mix of impurity phases and multiple spinel phases with higher temperature annealing. Furthermore, we demonstrate a 'continuous lattice' parameterization of the compositionally complex oxide structure provides a rapid means by which to examine the heterogeneity of the cation distribution through full profile refinement. The demonstrated tunability of the cation distribution or clustering in these compositionally complex spinels via thermodynamic levers affords interesting opportunities for rational design of functional materials.

Introduction

Nanostructured materials offer promising physicochemical properties across diverse applications in energy storage, sensing, catalysis, biomedicine, and more. Nano high entropy oxides (HEOs) and the more general class of compositionally complex oxides (CCOs) are expected to offer enhanced structure-property tunability by virtue of their large numbers of participating cations, their combined entropic disorder, and their intrinsic nano-size effects. HEOs are widely described as single-phase oxides that have five or more metal cations sharing a specific crystallographic lattice site in a random fashion. More stringent definitions add a criterion for configurational entropy (S_{config}) equal to or higher than $1.5R$ per mole of metals/cations, where R is the universal gas constant. In principle, the configurational entropy S_{config} can be tuned to achieve maximum site mixing at an equimolar ratio among the site sharing cations, allowing the entropic contribution (ΔS_{mix}) to the system energy to overcome competing enthalpic driving forces (ΔH_{mix}) with an increase in system temperature (T). According to the Gibbs free energy (ΔG_{mix}) formulation, $\Delta G_{mix} = \Delta H_{mix} - T\Delta S_{mix}$, a larger entropic term at higher temperature stabilizes the structure in a high entropy state, and the system is then termed an entropy stabilized oxide (ESO). However, in practice,

depending on the system, the maximized configurational entropy may not overcome the enthalpic energy with respect to alternate phase formation. Multiple factors in real systems contribute to the enthalpic term, including the specific cations incorporated, the preferred structural configuration (defects, distortions, specific patterns of chemical short-range order) associated with certain cations, the surface/interfacial energy, etc.[1–4] Many materials currently reported as HEOs and ESOs, some with novel and exceptional physical properties, do not meet the above thermodynamic criteria and likely feature cation configurations that are far from homogeneous and completely mixed.

Intentional efforts in designing and exploiting the wider class of CCOs can be embraced, including medium-entropy and non-equimolar composition oxides,[5] with the recognition that they provide even wider highly tunable phase space. For example, a number of recent works have highlighted the inherent flexibility and potential promise of exploring CCOs[5] by achieving low thermal conductivity and high stiffness among fluorite,[6,7] pyrochlore,[8–12] weberite, fergusonite,[9] and bixbyite[13] systems. A number of perovskite CCOs have shown promise as stable and high performing materials for energy storage/transformation applications.[14–16] These studies uncovered instances of property or structure tuning,[7–9,14,15] specific short-range order motifs,[7] order-disorder transformations,[10,11] multi-phase regions,[13] and other crystal-chemical phenomena.

Nano-size effects ubiquitous in nanosystems arise due to high surface area to volume ratios, non-equilibrium surface structures, unique shape/morphology, high interfacial energy, and more, offering further opportunities to explore phase space within the HEO/CCO paradigm. Limited work has been reported on nano-HEOs to date. Wang *et al.*[17] reported a nano-HEO material (Cu-Cr-Fe-Co-Ni-O) obtained via laser scanning ablation. Preparation of nano-fluorite HEO materials with ball-milling, chemical co-precipitation, and polymeric steric entrapment was reported by Jothi *et al.*[18] Nebulised spray pyrolysis, flame spray pyrolysis and reverse co-precipitation techniques were employed by Sarkar *et al.* to synthesize nanocrystalline rock salt structure HEOs.[19,20] Low-temperature solvothermal synthesis with

pyrolysis at 400°C was developed for obtaining nano-spinel structure HEOs by D. Wang *et al.*,[21] and the sol-gel method was used by G. Wang *et al.* to fabricate nano spherical mesoporous spinel HEO particles.[22] We note materials in these works have been reported as nano-HEOs (not nano-CCOs), though most do not explore/discuss specific thermodynamic criteria distinguishing them one way or the other.

Spinel Co_3O_4 is considered a favorable low temperature economical catalyst for formaldehyde oxidation, and variations are used in many other catalytic and electrochemical reactions.[23–26] For example, Co_3O_4 nanocrystals grown on reduced graphene oxide are high-performance bi-functional catalysts for the oxygen reduction reaction (ORR) (with reported overpotential of 310 mV) and oxygen evolution reaction (OER) (with reported onset potential of 0.82 V).[27] Furthermore, as one of the ferromagnetic metals (iron, nickel and cobalt) in nature, cobalt (Co) is essential to the development of hard magnetic materials due to its high saturation magnetization (M_S), high Curie temperature (T_C) and high magnetocrystalline anisotropy.[28] Most binary transition metal cobalt oxide spinels are earth abundant ferrimagnetic phases.[29–33]

In this work, a family of nano-$(nA_{1/n})Co_2O_4$ is synthesized by a low-temperature soft-templating (LTST) reaction route, where A includes n different equiatomic ratio $(1/n)$ combinations of 1 to 7 transition metal cations. Trends in phase selectivity and temperature stability are examined. The configurational entropy per mole of metals/cations (S_{config}) is smaller than $1.5R$ even if seven cations are sitting on the A site and all possible spinel configurations are assumed.[34] For example, the configurational entropies calculated for a normal spinel with formula ACo_2O_4 are 0.54R, 0.60R, and 0.65R for n=5, 6, and 7, respectively. The size/morphology, distribution of cations, and crystal structure within the nanostructures is examined via XRD, high resolution scanning-transmission electron microscopy/energy dispersive spectroscopy (STEM/EDS), and thermogravimetric analysis/differential scanning calorimetry (TGA/DSC) analysis. A new approach for obtaining nano/bulk structure information from CCOs with a 'continuous lattice' (CL) Rietveld refinement is also explored for

the first time.

Methods

Materials Synthesis

The LTST synthesis procedure used in this work is illustrated in Figure 1. The structur-

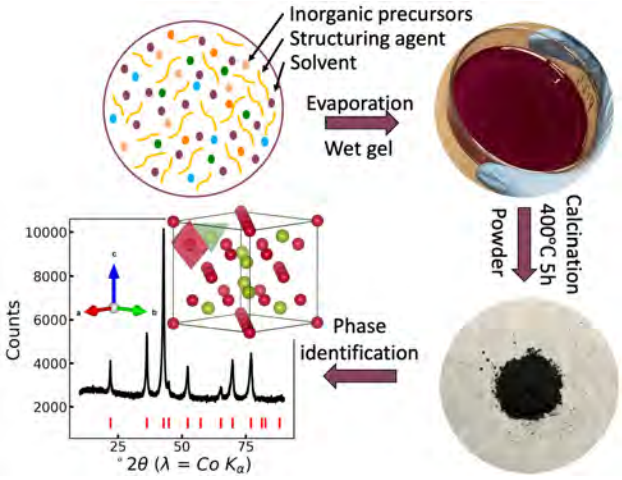

Figure 1: Schematic diagram of the LTST method used to synthesize a large family of compositionally complex cobalt-based nano spinels, $(nA_{1/n})Co_2O_4$. First, a solution of inorganic precursors, structuring agent, and solvent is stirred for 30 mins. A wet gel is obtained after 24 h evaporation and a black powder is formed after calcination at 400°C for 5h (the *as-formed* (AF) sample). Finally, a spinel phase structure with 8 tetrahedral (green) sites and 16 octahedral (red) sites in the unit cell is identified by XRD (oxygen atoms are not shown in the image).

ing agent [3.2g of Pluronic P123, a symmetric triblock copolymer comprising poly(ethylene oxide) (PEO) and poly(propylene oxide) (PPO) in an alternating linear fashion, PEO-PPO-PEO, ALDRICH Chemistry] was mixed in 20 mL Ethyl Alcohol (absolute, 200 Proof, 99.5+%, ACROS Organics). 0.5 mL Hydrochloric acid (HCl, Fisher Chemical) was added, and the mixture was stirred with a magnetic stir bar until Pluronic P123 was completely dissolved. Finally, a stoichiometric amount (1g $(nA_{1/n})Co_2O_4$ as the target) of inorganic nitrate hydrate precursor solutions in wt.% of metal were added into the solution. The nitrate hydrate sources are manganese nitrate tetrahydrate [$Mn(NO_3)_2{\cdot}4H_2O$, ACROS Organics],

iron chloride tetrahydrate ($FeCl_2{\cdot}4H_2O$, 99+%, ACROS Organics), nickel nitrate hexahydrate [$Ni(NO_3)_2{\cdot}6H_2O$, 98%, Alfa Aesar], zinc nitrate hexahydrate [$Zn(NO_3)_2{\cdot}6H_2O$, 99%, metal basis, Alfa Aesar], magnesium nitrate hexahydrate [$Mg(NO_3)_2{\cdot}6H_2O$, 99+%, ACROS Organics], cobalt nitrate hexahydrate [$Co(NO_3)_2{\cdot}6H_2O$, 99%, pure, ACROS Organics], and chromium nitrate nonahydrate [$Cr(NO_3)_3{\cdot}9H_2O$, 99%, ACROS Organics]. The entire mixed solution was stirred for 30 mins with a magnetic stirrer. The mixed solution was poured into a petri dish and evaporated under a fume hood for 24 h to obtain a wet gel. After evaporation, the gel was transferred to a furnace and calcined at 400°C for 5 h with a ramp rate of 1°C/min. The powder samples obtained via such steps without any further treatment are hereafter referred to as the *as-formed* (AF) samples. The majority of AF compositions in this work result in a spinel structure (SG 227, $Fd\bar{3}m$), as identified by XRD analysis (more details in Results section). Pellets of the AF samples were then made using a MP24A desktop pellet press and placed into the furnace for post-annealing heat treatment (*post-treatment*, PT) (at 600°C (PT6), 800°C (PT8), or 1000°C (PT10) for 5h and with a slow ramp rate of 2°C/min, 3°C/min, and 3°C/min, respectively). Sample compositions explored in this work with n of 5 or more are listed in Table 1, with corresponding XRD data shown in supplemental information (SI) Figure S1. Additional sample compositions are listed in SI: Table S1. Corresponding XRD data are shown in SI Figure S2. Sample names nCN reflect the number of n cations targeted (first character) and a specific Composition Number (CN), as summarized in Tables 1 and S1.

Characterization

X-ray Diffraction (XRD) Ambient XRD and high temperature XRD (HTXRD) data were measured using a PANalytical Empyrean diffractometer equipped with a Co X-ray source. Ambient XRD patterns were measured between 10 and 90° 2θ with a step size of 0.026°. HTXRD patterns were measured between 18 and 56° 2θ with a step size of 0.026° and acquisition time of 316 s at 11°C intervals from room temperature to 1000°C. The use of

Table 1: Compositions $(nA_{1/n})Co_2O_4$ with $n \geq 5$ explored within this work, separated into groups (see main text for details). Samples are observed after calcination (*as formed* 400°C, AF4) and following post-annealing heat treatment (*post-treatment* 600°C, PT6, etc.). Check marks indicate the presence of specific elements in each composition. Conditions resulting in X-ray pure phases are colored green and conditions resulting in phase mixtures are colored purple. Impurities are coded: CuO ("c"); rock salt ("r"); secondary spinel ("s"); and $CoCl_2 \cdot 2H_2O$ ("h").

Name	n	Mg	Cr	Mn	Fe	Co	Ni	Cu	Zn	AF4	PT6	PT8	PT10
Group 1: n=5 cation combinations													
5C1	5	✓		✓	✓			✓	✓			r	r+s
5C2	5			✓	✓		✓	✓	✓	h		c	c+r+s
5C3	5	✓		✓	✓		✓		✓			r	r+s
5C4	5	✓		✓			✓	✓	✓	r	r	r	r+s
5C5	5	✓			✓		✓	✓	✓	c+r	c+r	c+r	c+r
5C6	5	✓		✓	✓		✓	✓				r	r+s
Group 2: Increased number of cations (with Mg included)													
5C1	5	✓		✓	✓			✓	✓			r	r+s
6C1	6	✓		✓	✓		✓	✓	✓			r	r+s
7C1	7	✓	✓	✓	✓		✓	✓	✓			r	r+s
Group 3: Increased number of cations (without Mg included)													
5C2	5			✓	✓		✓	✓	✓	h		c	c+r+s
6C2	6			✓	✓	✓	✓	✓	✓				r+s
6C3	6		✓	✓	✓		✓	✓	✓				r+s
Group 4: n=5 cation combinations without Ni or Mg													
5C7	5			✓	✓	✓		✓	✓				c+s
5C8	5		✓	✓	✓			✓	✓				c+s

Co Kα radiation was essential to minimize fluorescence and uncover minor impurity phases.

Scanning Electron Microscopy/Energy Dispersive X-Ray Spectroscopy (SEM/EDS)

Specimens for scanning electron microscopy (SEM) and energy dispersive spectroscopy (EDS) were prepared by gently dispersing the ground powders onto a standard carbon tape. Zeiss Auriga high resolution SEM was used to characterize the morphologies of the specimens. Elemental analysis was carried out with a Zeiss EVO SEM.

Scanning-Transmission Electron Microscopy/Energy Dispersive Spectroscopy (STEM/EDS)

The morphology of the samples was investigated at the nanoscale by STEM imaging using a

JEOL JEM-2100F microscope operated at 200 kV. The chemical composition and elemental distribution of the samples were analyzed by energy dispersive X-ray spectroscopy (EDS) operated in scanning-transmission electron microscopy (STEM) mode (EDS 80 mm X-Max detector, Oxford Instruments). The STEM-EDS specimen preparation was carried out by sonication of powder samples in high purity propan-2-ol then drop-casted on copper grids coated with a holey carbon film (3.05 mm diam. 300 mesh, TAAB).

Thermogravimetric Analysis (TGA) and Differential Scanning Calorimetry (DSC)
The simultaneous measurement of weight change (TGA) and true differential heat flow (DSC) were examined by TA instuments SDT Q600 from ambient to 1000°C with a 5°C/min ramp rate in air.

Results and Discussion

Composition and Heat Treatment Effects

Nievely assuming a normal spinel structure, the tetrahedal site is occupied by the equimolar A^{2+} cations while the octahedral site is soley occupied by Co^{3+}. Figure 2 displays the calculated tolerance factor (top) and average ionic radii of tetrahedral site cations (bottom) resulting from these assumptions. Experimental conditions resulting in single phase spinel samples are indicated in green coloring while conditions resulting in samples containing secondary phases are indicated in purple coloring. Most compositions in the series result in a single phase spinel for AF4 and PT6 processing conditions (a), while the majority result in multiple or impurity phases for PT8 processing conditions (b). Dashed lines in the bottom plots indicate the specific participating ionic radii in each composition (again, nievely assuming a normal spinel configuration with strictly Co^{3+} and A^{2+} cations). All 12 compositions fall within the typical tolerance factor window for spinel oxides ($\sim$0.85),[35]

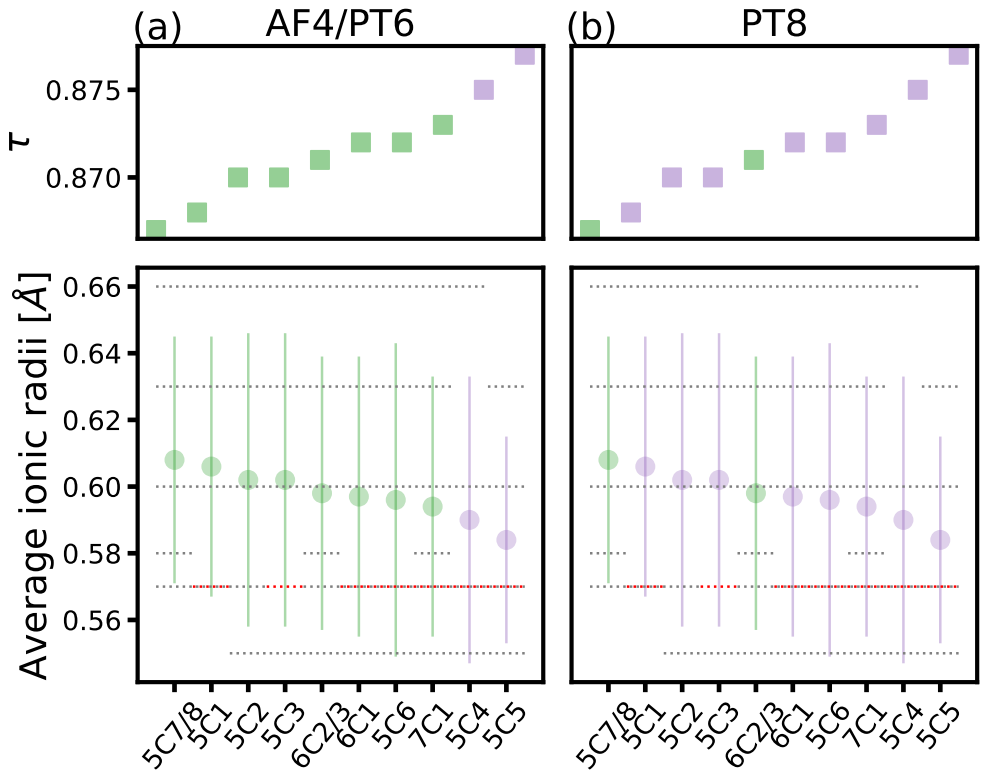

Figure 2: Spinel tolerance factore (τ) (top panels) and average ionic radii of tetrahedral site cations (bottom panels), assuming a normal spinel configuration, for (a) AF4 and PT6 samples, and (b) PT8 samples for each composition. Vertical lines in the bottom panels represent the calculated standard deviation of participating radii. The red dotted lines indicate the presence of "Mg" in a sample while black dotted lines indicate the presence of all other elements in the sample. Markers colored green indicate samples that appear X-ray phase pure. See Table 1 for sample compositions and further detail.

where the tolerance factor, τ, is defined

$$\tau = \frac{\sqrt{3}(R_{Co} + R_O)}{2(\langle R_A \rangle + R_O)}, \tag{1}$$

R_{Co} and R_O represent the ionic radiui of Co^{3+} and O^{2-}, and $\langle R_A \rangle$ represents the average radius of A^{2+}.

Table 1 lists all 5, 6, and 7 A-component compositions made in this work along with sample abbreviations used. All *as-formed* and *post-treatment* samples were screened with XRD analysis to assess phase identity, phase purity, degree of crystallinity, and (to the extent possible) cation site inversion, γ. Representative data are shown in SI Figure S1 for

all samples. Rietveld refinement (discussed below) was used to confirm secondary phases and estimate phase impurity levels. In Table 1 and Figure 2 synthesis conditions resulting in single spinel phases are indicated with green coloring, while those resulting in impurity phases (either cobalt chloride hydrate (h), rock salt (r), tenorite CuO (c), or secondary spinel phase (s)) are indicated in purple coloring.

A few details are immediately apparent. First, many of the compositions in this work result in single phase spinel oxides in their *as-formed* state. To the best of our knowledge, these CCOs are reported here for the first time. Figure 2 reveals that the average ionic radii of the A site cations (and the corresponding spinel tolerance factor) plays a key role in determining which compositions will form a single phase spinel in AF4 and PT6 samples. Samples with tolerance factors below 0.874 (assuming a normal spinel structure) result in a single spinel phase. Those with larger tolerance factors result in impurity phases, primarily including rock salt AO or tenorite CuO phases.

Second, the spinel oxides in this work are metastable; when processed at 1000°C, the spinel phase segregates into multiple spinel phases (the secondary spinel phase is indicated by "s" in Table 1). This segregation is also corroborated by the STEM-EDS analysis presented below, indiciating segregation of Fe and Mn relative to other A site atoms. In Group 1 (n=5 cation combinations) of Table 1, *5C5*, does not contain Mn and does not result in a secondary spinel phase for PT10 conditions. Conversely, compositions *2C4* (A= Fe and Zn) and *2C5* (A= Mn and Zn) (listed in SI Table S1, and representative data shown in SI Figure S2) exhibit a secondary spinel phase for PT10 conditions. This suggests that regardless of any other component present, Mn consistently prefers to segregate to a secondary spinel phase, while Fe's behavior depends on the other components involved. This observation is reasonable given that tetrahedrally coordinated Mn and Fe possess larger ionic radii (0.66 Å for Mn^{2+} and 0.63 Å for Fe^{2+}) in comparison to other components (as illustrated in the bottom panels of Figure 2).

Thirdly, Table 1 and Figure 2 reveal that the number of cations participating, represented

by n, is just one of several considerations in phase stability and selection in the PT8 series. Which cations are present can play a dominant role. Take, for instance, Group 2 (Increased number of cations, with Mg included) and Group 3 (Increased number of cations, without Mg included) in Table 1: the incorporation of Mg in the A site results in a smaller thermal stability window for the CCO spinel phases. When Mg is left out, additional cations result in a wider thermal stability window for a single CCO spinel phase. The presence of Mg over-rides the influence of increasing n in the compositions explored.

Further, in SI Table S1, compositions *2C1* (A= Mg and Zn), *2C3* (A= Ni and Zn), *4C1* (A= Mg, Mn, Fe, and Zn) and *4C2* (A= Mn, Fe, Ni and Zn) all result in rock salt impurities for PT10 conditions (representative data are shown in SI Figure S2). These samples all contain Mg or Ni. Mg shows high favorability for the rock salt phase formation; for example, the study of *4C1* shows a tiny rock salt impurity peak in PT8 while *4C2* does not (see SI Figure S2). Based on these results, samples *5C7* and *5C8* in Group 4 (without Ni or Mg) in Table 1 were designed and synthesized without impurity phases under PT8 conditions. All of these results support the conclusion that the incorporation of Mg or Ni contributes to rock salt AO impurity formation.

The phase formation energies of possible binary impurities (known binary oxides of cations involved) are shown in Figure 3, arranged by cation valence state. The information provides some thermodynamic rationale for the specific impurity phases encountered in our study. As mentioned above, all compositions containing Ni or Mg lead to rock salt impurities with heat treatment. Tenorite-line (CuO) formation appears in sample *2C2* (A= Cu and Zn, AF4, PT6, PT8, and PT10), *5C2* (PT8 and PT10), *5C5* (AF4, PT6, PT8, and PT10), *5C7* (PT10) and *5C8* (PT10). The phase formation energies for 2+ cations shown in Figure 3 range between -601.6 kJ/mol for rock salt MgO[36] and -157.3 kJ/mol[36] for tenorite CuO. We note Ni, Mg, and Cu are notably absent in the group of mixed valent A_3O_4 spinels, which included the Co, Fe, Cr, and Mn cases (appearing at the far right of Figure 3). Such findings infer the importance of cation selection in determining the structural stability and

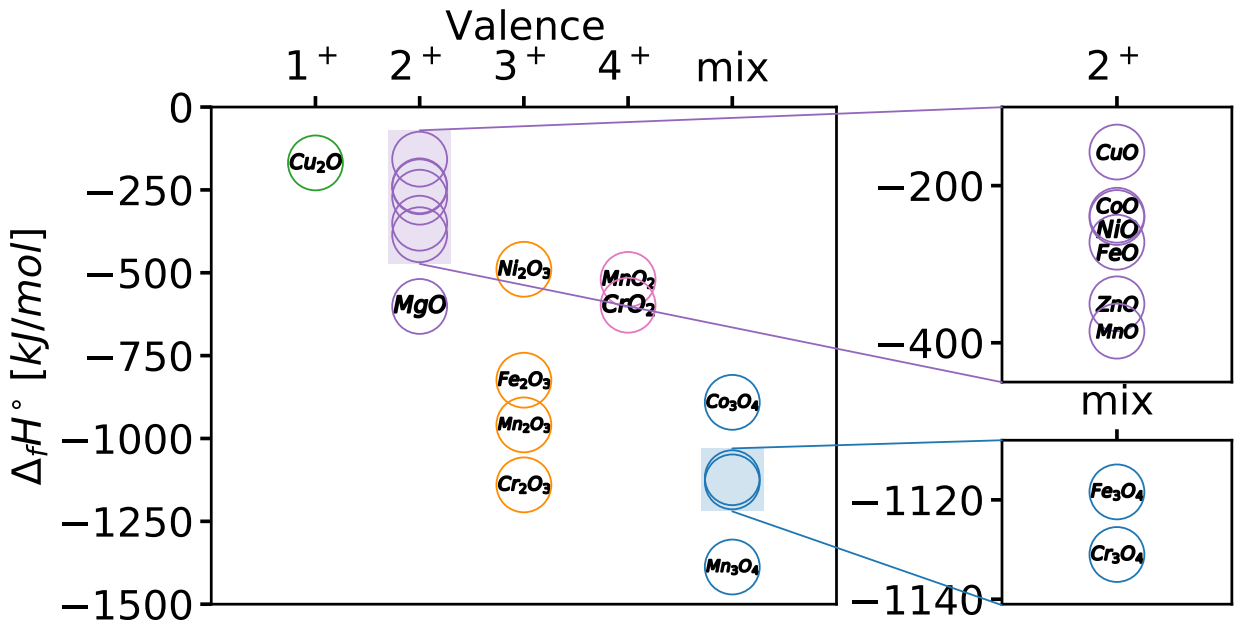

Figure 3: Phase formation energy, ΔH_f°, for possible binary oxide impurities resulting from the inclusion of single cations with different oxidation states.

impurity phase formation.

The impurity phases found here with higher *post-treatment* temperature are counter indicative of the entropy stabilization effect – increasing the *post-treatment* temperature is expected to enhance the entropic contribution ($-T\Delta S_{mix}$) to the overall Gibbs free energy and hence is expected to favor the structure of a single phase. Therefore, other factors contribute to the lowering of mixing (i.e., diminishing the effect of the configurational entropy) at high temperatures. Compositional heterogeneity is therefore an important factor to consider in the *post-treatment* procedure.

Case Study: $(Mg_{0.2}Mn_{0.2}Fe_{0.2}Cu_{0.2}Zn_{0.2})Co_2O_4$ (5C1)

Phase Formation

Composition *5C1* presents a single phase spinel structure for AF4 and PT6 conditions, but is observed to separate into a spinel with MgO impurity for PT8 conditions and exhibit a second (Mn and Fe rich) spinel phase for PT10 conditions. This solid-state phase transformation

process was examined in greater detail using in-situ HTXRD and TGA/DSC (Figure 4). A reconstructive phase transformation from spinel to rock salt begins around 714 °C and is nearly complete around 1100°C. Upon slow cooling, the rock salt phase decomposes into two spinels phases and a remnant rock salt phase. The irreversible phase transformation confirms that the initial spinel *5C1* is metastable.

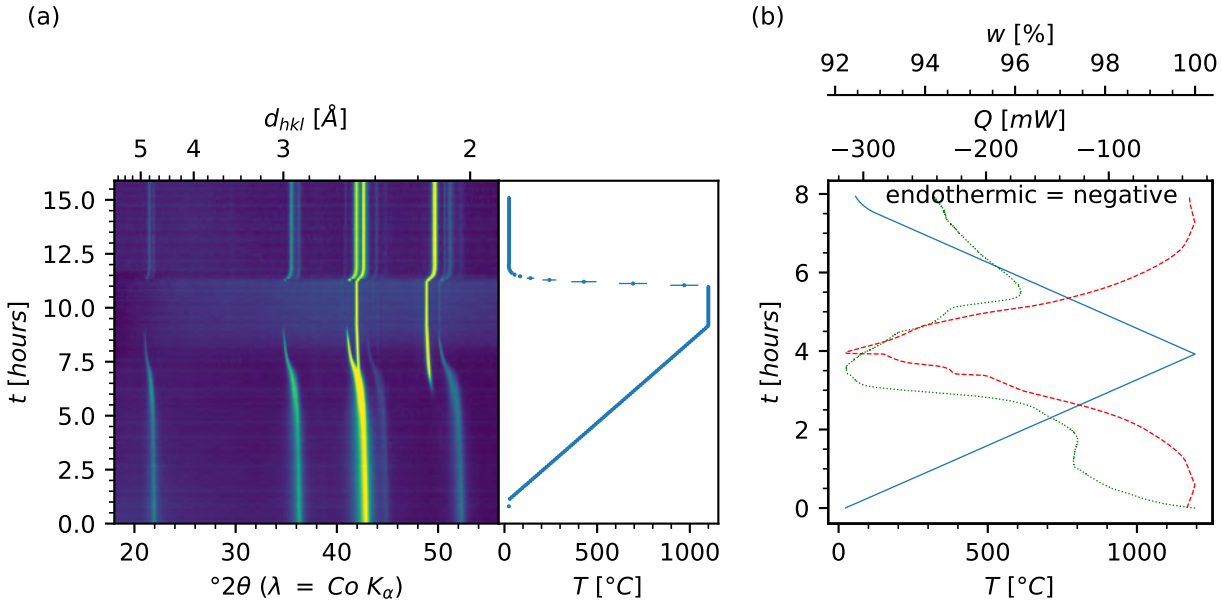

Figure 4: (a) Logarithmic powder diffraction intensities collected step-wise in 11 °C intervals to 1100 °C, over an isothermal dwell, and free-cooling to room temperature. (b) Thermal analysis signals collected over a heating and cooling cycle with 300 °C/h ramp rate: temperature (blue —), weight change (green · · ·), and heat flow (red - - -).

Throughout this thermal cycle the heat flow is endothermic. The phase transformation from spinel (4:3 O:A) to rock salt (1:1 O:A) is accompanied by a corresponding loss of oxygen. For *5C1* reduction to a stoichiometric rock salt formula corresponds with a 6.8% mass loss. In the measured weight loss, initial heating results in a 2.5% weight loss, likely due to adsorbed water and surface hydroxyls, and subsequent 5.3% weight loss. Faint diffraction intensity corresponding to a spinel is present with the rock salt Bragg peaks above 1100 °C. Together, this suggests some phase coexistence and perhaps oxygen nonstoichiometry.

For rock salt and for distinct spinel phases to form we propose the phase transformation must be diffusional, though over different characteristic lengths for the oxygen and anion

substructures. The transformation from spinel to rock salt is well known, for instance in the Li-Mn-N-O system,[37] where delithiation of the spinel results in rock salt formation. Transformation between the two structures effectively constitutes ordering of cation vacancies and interstitials. Meanwhile, a change in oxygen stoichiometry implies oxygen diffusion from the bulk to the powder surface. Thus, recovery of the spinel upon cooling is expected to have a kinetic limitation dependent upon temperature and ambient oxygen partial pressure. Together, this analysis implies that the *as-formed* spinel is metastable. Further evidence for incipient cation segregation in the metastable *as-formed* spinel is presented below.

Microscopy

SEM images corresponding to the *5C1* sample series (AF4, PT6, PT8, PT10) are depicted in SI Figure S4. Notably, the AF4 sample exhibits a wide particle size distribution (ranging from 10 to 100 nm). This finding is in agreement with the XRD results shown in SI Figure S1, where the AF4 sample exhibits a stronger peak asymmetry. Peak width and asymmetry decrease in PT6 and PT8 samples, indicating that higher *post-treatment* temperature results in larger particle sizes and a more homogeneous particle size distribution. The PT10 sample exhibits micron scale particle size. SEM/EDS characterization revealed that sample *5C1* AF4 is microscopically homogeneous in terms of cation composition (depicted in SI Figure S3).

The distribution of various elements among particles or domains was investigated at high resolution using STEM/EDS elemental mapping as depicted in Figure 5. Interestingly, the degree of heterogeneity is found to vary significantly in the *5C1* sample series on the nanoscale. In Figure 5 AF4, notable enrichment of Mg and Mn in specific grains is evident, along with a less severe enrichment of Fe. In PT6 and PT8 samples, the cation enrichments fade (samples feature more homogeneous cation distributions). At higher *post-treatment* temperatures, multiple phases are observed. In PT10, the migration of Mn, Fe, and Mg was observed to have occurred entirely out of some grains, while the enrichment of Co in select

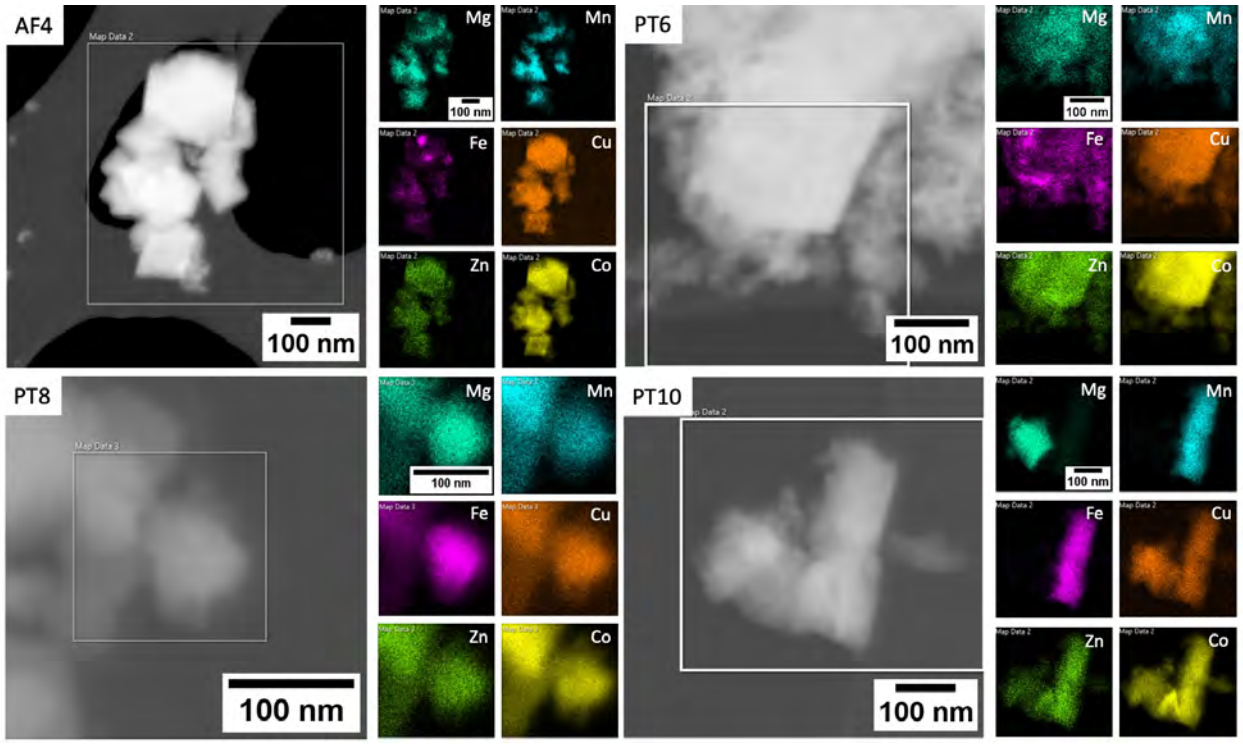

Figure 5: STEM/EDS elemental mapping of *5C1* AF4, PT6, PT8, and PT10 samples. Color maps indicate heterogeneous cation distributions of Mg, Mn and Fe for certain grains in the AF4 sample. In PT6 and PT8 samples, the cation enrichments fade (samples feature more homogeneous cation distributions). In the PT10 sample, Mn and Fe atoms are found in separate grains from Mg, and a modest enrichment of Co is observed in those grains with Mn and Fe. Cu and Zn remain distributed throughout all particles.

grains persisted.

Rietveld Analysis

Visual inspection of the XRD pattern in SI Figure S1 for *5C1* AF4 reveals broad and asymmetric diffraction peaks. The complex microstructure of the samples can be investigated in part by refinement of Bragg diffraction profiles. Conventional Rietveld refinement approaches were first tried and typical results are presented in Figure 6 (a) to (c). Refinement results for models incorporating crystallite size broadening (Figure 6 a), size and strain broadening (Figure 6 b), or two spinel phases (with unique phase fractions and lattice parameter, all other values constrained equal) (Figure 6 c) are shown for *5C1* AF4. Here, the random spinel structure was selected as the basis since it fits the phase better compared to the normal and inverse spinel structures. Models incorporating size and strain effects poorly fit the peak profile shapes. A two-phase model, on the other hand, provides a marked improvement in the quality of fit (R_{wp}=2.171%). This fit incorporates an additional phase fraction parameter and lattice parameter. Since we do not know the distribution of atoms residing within the potential multiple phases, the phase fraction provides limited information.

Spatially varying scalar variables, like occupancy, can result in asymmetric line broadening like that observed here. The resulting line broadening will have a profile proportional to the probability density function of the scalar variable, and anisotropy proportional to the resultant lattice strain.[39] In the case that the scalar variable is normally distributed and the resulting strain is isotropic, conventional microstrain broadening is recovered. Otherwise, a suitable probability density function must be derived or guessed. For example, earlier work by Leineweber[40,41] employed an Edgeworth series to approximate non-Gaussian N distribution in ϵ-FeN$_y$.

In this case, we do not know a priori what probability density function to assume, and we are not interested in the anisotropy of the strain response, but rather are interested in estimating the probability density function of the compositional fluctuation within coher-

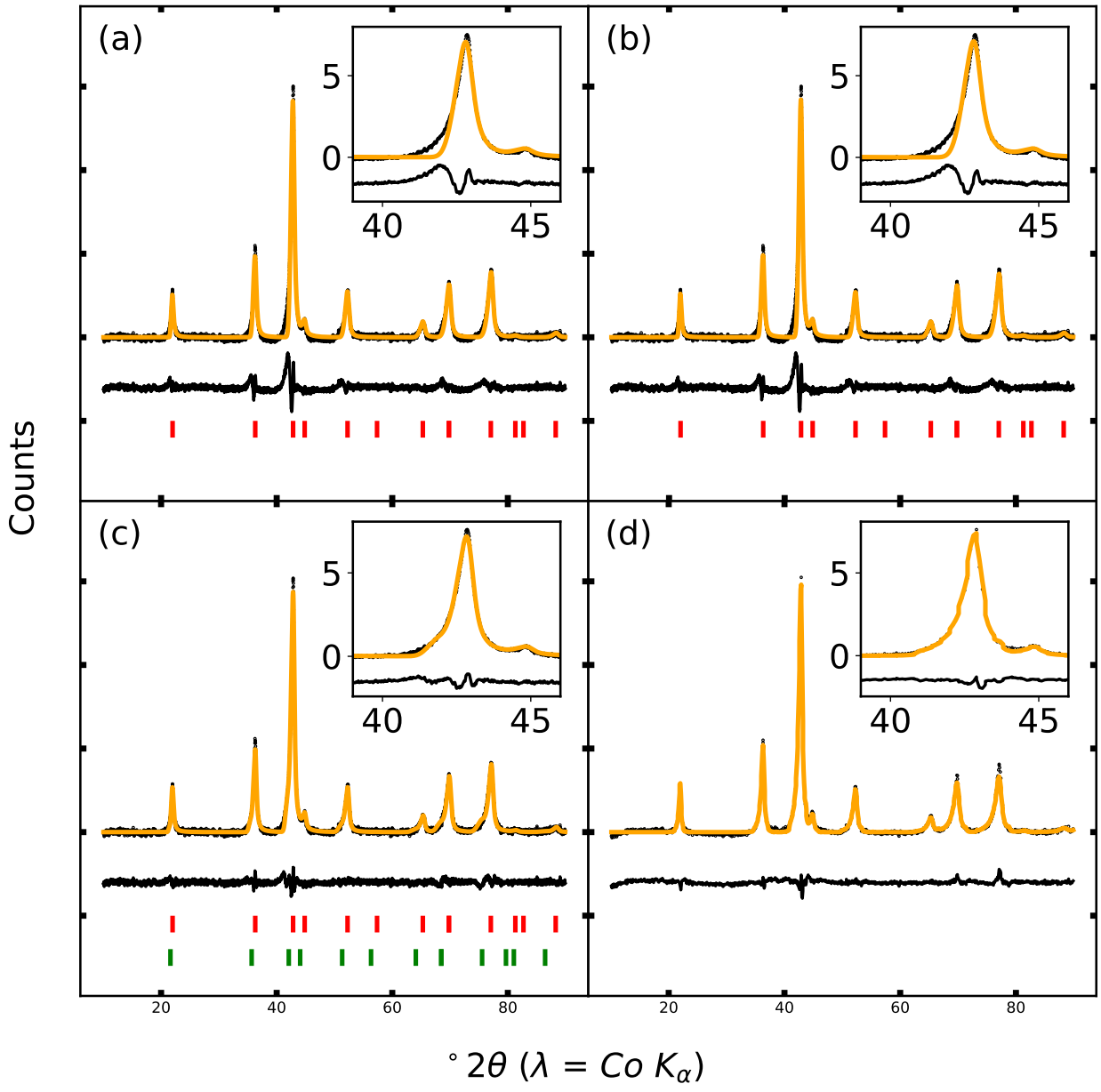

Figure 6: Rietveld refinements for *5C1* AF4 X-ray diffraction data with (a) crystalline grain size broadening (1 phase, no strain, $R_{wp} = 3.870\%$), (b) size and strain broadening (1 phase, refined strain, $R_{wp} = 3.869\%$), (c) two spinel phase model (phase fraction and cubic lattice parameter refined, no strain, $R_{wp} = 2.171\%$), and (d) CL phase model ($R_{wp} = 2.113\%$) applied. The XRD patterns were analyzed with the Rietveld method as embodied in the TOPAS-V7[38] program.

ently diffracting crystallite domains. Further, because we are insensitive to atom type, the distribution in question is further collapsed to fluctuation of atomic radius around its mean value. To this end, we constructed what we have termed a CL model embedding isotropic lattice strain by superimposing a hierarchically constrained set of phases of discrete volume.

In this scheme, N identical crystal phase models are instantiated with fixed lattice volumes spanning the average observed value. Each model is given a refinable scale parameter (s_i), however each value is constrained by a weighted (w_i) penalty (p)

$$p = \Sigma_i w_i \sqrt{(s_{i+1} - s_i)^2}, \tag{2}$$

such that neighboring values cannot differ significantly, resulting in a locally linear or smoothly varying distribution. Because extraneous instrumental line broadening is controlled for, the resulting distribution of s_i should closely resemble the unknown distribution of the atomic radii. As shown in Figure 6 (d), the overall agreement with the experimental diffraction pattern was significantly improved ($R_{wp} = 2.113\%$). This parameterization of the CCO structure provides a rapid means by which to examine the heterogeneity of the A-site cation distribution through full profile refinement, as demonstrated in the following section.

Line Profile Analysis as a Screening Tool

Asymmetric peak shapes observed in data cannot be adequately explained by conventional microstrain models and crystallite size models, which assume symmetric intensity distributions. To address this misfit, there is a need for an asymmetric line broadening mechanism. The CL model with inhomogeneous cation distribution (and lattice volume) constructs the total intensity by a weighted sum of phases, and is proposed here as a powerful screening tool for analysis of microstrain-like line-broadening data, like nano-materials. By properly characterizing and modeling the peak profile of microstrain-like data, more reliable and relevent crystallographic information can be obtained.

By applying the CL phase to all $(nA_{1/n})Co_2O_4$ ($n \geq 5$) AF4, PT6, and PT8 samples (Representative data are shown in SI Figure S1), the A-site (tetrahedral site) ionic radius distribution can be extracted from lattice parameters and atomic positions. The distribution of lattices is seen to decrease (from left to right) with increasing *post-treatment* temperature, shown in Figure 7. This finding confirms the conclusion already suggested by the XRD, SEM, and TEM results, that the samples formed at low-T have broad asymmetric intensity distributions, inferring spatially heterogeneous cation distributions. Samples that experienced *post-treatment* feature increasingly sharp and symmetric diffraction peaks, inferring less heterogeneity of the cation distribution. At higher *post-treatment* temperatures, temperature activiated de-mixing leads to multiple distinct spinel phases. Together, this suggests the *as-formed* spinel is kinetically stabilized and possesses local chemical ordering.

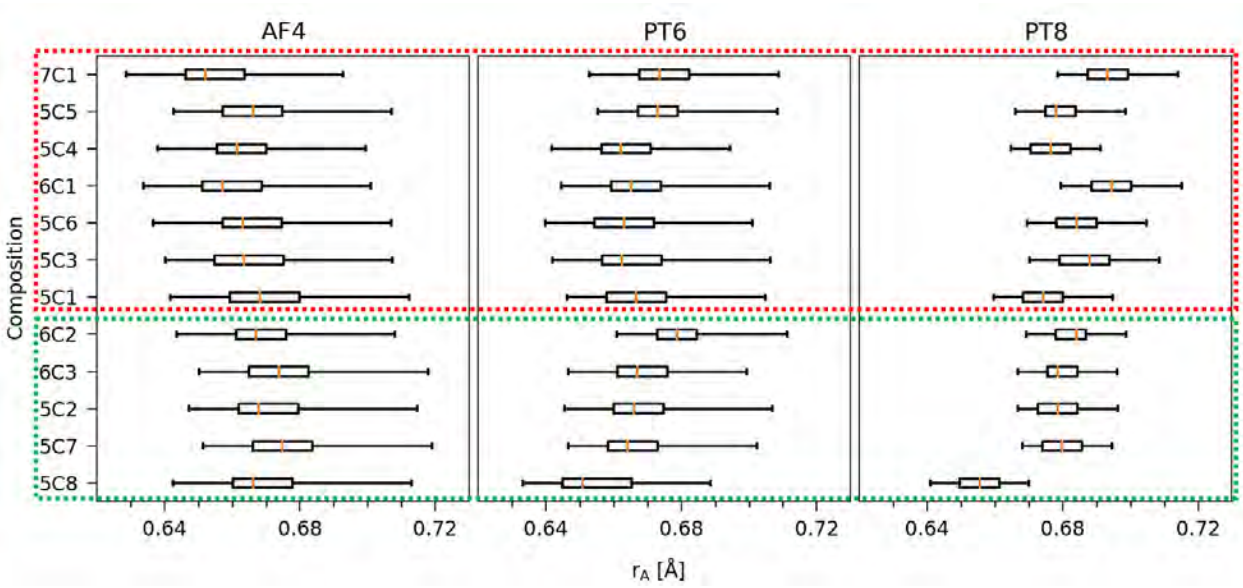

Figure 7: Tetrahedral site ionic radius (r_A) distribution extracted from CL Rietveld refinement results for $(nA_{1/n})Co_2O_4$ ($n \geq 5$) samples. The heat treatment conditions are listed at the top of each column, while the composition identities of each series is shown on the left of each row. The compositions are ordered by increasing calculated average octahedral site radius (where an inverse spinel structure is assumed) and calculated average tetrahedral site radius (where a normal spinel structure is assumed) for the compositions in the red box and green box, respectively.

Interestingly, an exampination of the degree of inversion (the fraction of A-site ions

occupying the octahedral sites),[34] γ, extracted from CL refinements groups the samples into two categories: those incorporating Mg (represented by red squares in Figure 7) and those without Mg (represented by green squares in Figure 7). In Figure 8, the inversion parameter γ in *as-formed* samples is found to be relatively random. With increasing *post-treatment* temperature the compositions containing Mg (highlighted in red) trend towards an inverse structure, while those without Mg (highlighted in green) trend towards a normal spinel structure.

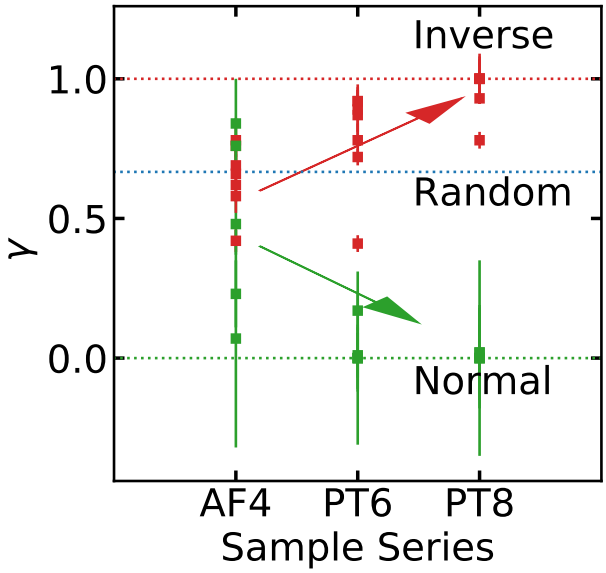

Figure 8: The degree of inversion, γ, for samples $(n\mathrm{A}_{1/n})\mathrm{Co_2O_4}$ ($n \geq 5$), obtained from CL refinements, with error bars included. The heat treatment condition for each sample is listed on the x-axis. The samples are grouped into two categories: those with Mg in the compositions (represented by red squares) and those without Mg in the composition (represented by green squares). The red and green arrows indicate the structural trend observed with increasing *post-treatment* temperature.

In Figure 7 we have ordered compositions from top to bottom in order of increasing predicted average octahedral ionic radius (assuming the detected inverse spinel structure model for compositions highlighted in red), and increasing tetrahedral ionic radius (assuming the detected normal spinel structure model for compositions highlighted in green). The lack of clear trends with respect to average predicted site radii implies that additional factors (cation valence, nanoscale segregated phases, oxygen defects, etc.) play roles in directing

crystal-chemical trends in this series. In conclusion, line profile analysis, along with the CL model, is a valuable tool for screening material structure variations in compositional and processing condition series. Further investigations are necessary to better understand the impact of cation distribution on chemical short-range order in this series of spinel oxides.

Conclusion

This work has elucidated that the LTST method successfully results in single phase CCO spinels $(n\mathrm{A}_{1/n})\mathrm{Co}_2\mathrm{O}_4$ with high surface areas and heterogeneous microstructures that can be tuned with *post-treatment*. At least 12 distinct $\mathrm{ACo}_2\mathrm{O}_4$ samples were identified with four or more equimolar A cations in this work: a great number more are likely feasible through alternate or non-equimolar A cation combinations. The CCOs are all found to be metastable, partitioning into two distinct spinel phases upon *post-treatment* at 1000°C (or lower). It was found that phase selection and stability are impacted by both which cation species are present and how many cation species are included. When Mg or Ni are present in the compositional series, the lower enthalpy of formation of MgO (in PT8 and PT10) and NiO (in PT10) dominates, resulting in CCO spinels with rock salt phase impurities. It was found that the onset of rock salt impurity phase with increasing calcination temperature can be suppressed or eliminated in samples without Mg by increasing the number n of participating cations in the series.

A detailed characterization of *5C1* via in situ HTXRD, SEM/EDS, STEM/EDS, and Rietveld refinement uncovers significant and varying cation segregation in AF4, PT6, PT8, and PT10 samples. *Post-treatment* is seen to effectively redistribute A-site cation short-range order, in an important confirmation of the ability to tune lattice heterogeneity in this family of medium entropy spinel oxides. We demonstrated that CL model refinements are adept at capturing the unusual diffraction peak profiles of CCOs in this series. We utilized the models to demonstrate that an intermediate processing temperature gives rise to more

compositionally homogenous CCOs in our series. It is anticipated such models will find wide use in the structural description of HEOs, ESOs, and CCOs, providing much-needed descriptors of the intrinsic lattice strain, nano-segregated phases, and multi-structured natures apt to be present and key to material properties in these series. Overall, this work demonstrates there are many potentially interesting metastable nanophases that can be prepared via LTST methods in this compositional series, and that there is great potential for tuning their morphologies and atomic structures.

Acknowledgement

This work is primarily supported by NSF-DMR-2145174. Materials synthesis efforts by Xin Wang were supported in part by UT-ORII Seed Funding. Contributions of Prof. Eric Lass (thermodynamic discussions) were supported by NSF-DMR-1408722 and contributions of Dr. Eleonora Calì (STEM/EDS) were supported by the EPSRC grant EP/R023522/1. X-ray diffraction data was collected at the Core Facility at the Institute for Advanced Materials and Manufacturing (IAMM) at the University of Knoxville, Tennessee. The authors gratefully acknowledge Dr. Michael Koehler for his assistance with XRD measurements reported in this work.

Supporting Information Available

The following file is available free of charge. *Supplemental Information: Phase Selectivity and Stability in Compositionally Complex Nano* $(nA_{1/n})Co_2O_4$: XRD patterns following different heat treatments for all compositions studied in this work, a table containing compositions and purity/impurity phases of samples with n$\leq$4, SEM/EDS images for sample $5C1$ AF4, and SEM images of samples $5C1$, $6C1$, and $7C1$ prepared AF4, PT6, PT8, and PT10.

References

(1) Spurling, R. J.; Lass, E. A.; Wang, X.; Page, K. Entropy-driven phase transitions in complex ceramic oxides. *Physical Review Materials* **2022**, *6*, 090301.

(2) Sarkar, A.; Wang, Q.; Schiele, A.; Chellali, M. R.; Bhattacharya, S. S.; Wang, D.; Brezesinski, T.; Hahn, H.; Velasco, L.; Breitung, B. High-entropy oxides: fundamental aspects and electrochemical properties. *Advanced Materials* **2019**, *31*, 1806236.

(3) Sarkar, A.; Breitung, B.; Hahn, H. High entropy oxides: the role of entropy, enthalpy and synergy. *Scripta Materialia* **2020**, *187*, 43–48.

(4) McCormack, S. J.; Navrotsky, A. Thermodynamics of high entropy oxides. *Acta Materialia* **2021**, *202*, 1–21.

(5) Wright, A. J.; Luo, J. A step forward from high-entropy ceramics to compositionally complex ceramics: a new perspective. *Journal of Materials Science* **2020**, *55*, 9812–9827.

(6) Wright, A. J.; Wang, Q.; Huang, C.; Nieto, A.; Chen, R.; Luo, J. From high-entropy ceramics to compositionally-complex ceramics: A case study of fluorite oxides. *Journal of the European Ceramic Society* **2020**, *40*, 2120–2129.

(7) Wright, A. J.; Wang, Q.; Yeh, Y.-T.; Zhang, D.; Everett, M.; Neuefeind, J.; Chen, R.; Luo, J. Short-Range Order and Origin of the Low Thermal Conductivity in Compositionally Complex Rare-Earth Niobates and Tantalates. *Acta Materialia* **2022**, 118056.

(8) Wright, A. J.; Wang, Q.; Ko, S.-T.; Chung, K. M.; Chen, R.; Luo, J. Size disorder as a descriptor for predicting reduced thermal conductivity in medium-and high-entropy pyrochlore oxides. *Scripta Materialia* **2020**, *181*, 76–81.

(9) Qin, M.; Vega, H.; Zhang, D.; Adapa, S.; Wright, A. J.; Chen, R.; Luo, J. 21-Component compositionally complex ceramics: Discovery of ultrahigh-entropy weberite and fer-

gusonite phases and a pyrochlore-weberite transition. *Journal of Advanced Ceramics* **2022**, *11*, 641–655.

(10) Wright, A. J.; Wang, Q.; Hu, C.; Yeh, Y.-T.; Chen, R.; Luo, J. Single-phase duodenary high-entropy fluorite/pyrochlore oxides with an order-disorder transition. *Acta Materialia* **2021**, *211*, 116858.

(11) Zhang, D.; Chen, Y.; Feng, T.; Yu, D.; An, K.; Chen, R.; Luo, J. Discovery of a reversible redox-induced order-disorder transition in a 10-component compositionally complex ceramic. *Scripta Materialia* **2022**, *215*, 114699.

(12) Zhang, D.; Chen, Y.; Vega, H.; Feng, T.; Yu, D.; Everett, M.; Neuefeind, J.; An, K.; Chen, R.; Luo, J. Long-and short-range orders in 10-component compositionally complex ceramics. *Advanced Powder Materials* **2023**, *2*, 100098.

(13) Vega, H.; Qin, M.; Luo, J. Thermodynamics of dual-phase compositionally complex ceramics: A case study of ultrahigh-entropy fluorite-bixbyite refractory oxides. *Journal of the European Ceramic Society* **2023**, *43*, 2104–2114.

(14) Ko, S.-T.; Lee, T.; Qi, J.; Zhang, D.; Peng, W.-T.; Wang, X.; Tsai, W.-C.; Sun, S.; Wang, Z.; Bowman, W. J., et al. Compositionally Complex Perovskite Oxides as a New Class of Li-Ion Solid Electrolytes. *arXiv preprint arXiv:2212.13451* **2022**, 1–28.

(15) Zhang, D. et al. Compositionally Complex Perovskite Oxides for Solar Thermochemical Water Splitting. *Chemistry of Materials* **2023**, *35*, 1901–1915.

(16) Zhang, D.; Park, J.; Xu, B.; Liu, C.; Li, W.; Liu, X.; Qi, Y.; Luo, J. Unusual aliovalent doping effects on oxygen non-stoichiometry in medium-entropy compositionally complex perovskite oxides. *Dalton Transactions* **2023**, *52*, 1082–1088.

(17) Wang, B.; Wang, C.; Yu, X.; Cao, Y.; Gao, L.; Wu, C.; Yao, Y.; Lin, Z.; Zou, Z. Gen-

eral synthesis of high-entropy alloy and ceramic nanoparticles in nanoseconds. *Nature Synthesis* **2022**, *1*, 138–146.

(18) Jothi, P. R.; Liyanage, W.; Jiang, B.; Paladugu, S.; Olds, D.; Gilbert, D. A.; Page, K. Persistent Structure and Frustrated Magnetism in High Entropy Rare-Earth Zirconates. *Small* **2022**, *18*, 2101323.

(19) Sarkar, A.; Djenadic, R.; Usharani, N. J.; Sanghvi, K. P.; Chakravadhanula, V. S.; Gandhi, A. S.; Hahn, H.; Bhattacharya, S. S. Nanocrystalline multicomponent entropy stabilised transition metal oxides. *Journal of the European Ceramic Society* **2017**, *37*, 747–754.

(20) Zhang, R.-Z.; Reece, M. J. Review of high entropy ceramics: design, synthesis, structure and properties. *Journal of Materials Chemistry A* **2019**, *7*, 22148–22162.

(21) Wang, D.; Liu, Z.; Du, S.; Zhang, Y.; Li, H.; Xiao, Z.; Chen, W.; Chen, R.; Wang, Y.; Zou, Y.; Wang, S. Low-temperature synthesis of small-sized high-entropy oxides for water oxidation. *Journal of Materials Chemistry A* **2019**, *7*, 24211–24216.

(22) Wang, G.; Qin, J.; Feng, Y.; Feng, B.; Yang, S.; Wang, Z.; Zhao, Y.; Wei, J. Sol–gel synthesis of spherical mesoporous high-entropy oxides. *ACS Applied Materials & Interfaces* **2020**, *12*, 45155–45164.

(23) Li, R.; Huang, Y.; Zhu, D.; Ho, W.; Lee, S.; Cao, J. A Review of Co_3O_4-based Catalysts for Formaldehyde Oxidation at Low Temperature: Effect Parameters and Reaction Mechanism. *Aerosol Science and Engineering* **2020**, *4*, 147–168.

(24) Shetgaonkar, S. S.; Salkar, A. V.; Morajkar, P. P. Advances in Electrochemical and Catalytic Performance of Nanostructured $FeCo_2O_4$ and Its Composites. *Chemistry–An Asian Journal* **2021**, *16*, 2871–2895.

(25) Gonçalves, J. M.; Rocha, D. P.; Silva, M. N.; Martins, P. R.; Nossol, E.; Angnes, L.; Rout, C. S.; Munoz, R. A. Feasible strategies to promote the sensing performances of spinel MCo_2O_4 (M= Ni, Fe, Mn, Cu and Zn) based electrochemical sensors: a review. *Journal of Materials Chemistry C* **2021**, *9*, 7852–7887.

(26) Wu, R.; Sun, J.; Xu, C.; Chen, H. $MgCo_2O_4$-based electrode materials for electrochemical energy storage and conversion: a comprehensive review. *Sustainable Energy & Fuels* **2021**, *5*, 4807–4829.

(27) Liang, Y.; Li, Y.; Wang, H.; Zhou, J.; Wang, J.; Regier, T.; Dai, H. Co_3O_4 nanocrystals on graphene as a synergistic catalyst for oxygen reduction reaction. *Nature materials* **2011**, *10*, 780–786.

(28) Mohapatra, J.; Xing, M.; Elkins, J.; Liu, J. P. Hard and semi-hard magnetic materials based on cobalt and cobalt alloys. *Journal of Alloys and Compounds* **2020**, *824*, 153874.

(29) Borges, F.; Melo, D.; Câmara, M.; Martinelli, A.; Soares, J.; De Araujo, J.; Cabral, F. Magnetic behavior of nanocrystalline $MnCo_2O_4$ spinels. *Journal of magnetism and magnetic materials* **2006**, *302*, 273–277.

(30) Bitla, Y.; Chin, Y.-Y.; Lin, J.-C.; Van, C. N.; Liu, R.; Zhu, Y.; Liu, H.-J.; Zhan, Q.; Lin, H.-J.; Chen, C.-T., et al. Origin of metallic behavior in $NiCo_2O_4$ ferrimagnet. *Scientific reports* **2015**, *5*, 1–8.

(31) Kawano, S.; Achiwa, N.; Yamamoto, N.; Higashi, S.-n. Metal-ion distribution and magnetic structure of Fe-substituted cobaltite spinel: $FeCo_2O_4$. *Materials Research Bulletin* **1976**, *11*, 911–916.

(32) Nakhowong, R.; Chueachot, R. Synthesis and magnetic properties of copper cobaltite ($CuCo_2O_4$) fibers by electrospinning. *Journal of Alloys and Compounds* **2017**, *715*, 390–396.

(33) Yagi, S.; Ichikawa, Y.; Yamada, I.; Doi, T.; Ichitsubo, T.; Matsubara, E. Synthesis of binary magnesium–transition metal oxides via inverse coprecipitation. *Japanese journal of applied physics* **2013**, *52*, 025501.

(34) Wang, X.; Musicó, B. L.; Kons, C.; Metz, P. C.; Keppens, V.; Gilbert, D. A.; Zhang, Y.; Page, K. Local cation order and ferrimagnetism in compositionally complex spinel ferrites. *APL Materials* **2022**, *10*, 121102.

(35) Song, Z.; Liu, Q. Tolerance factor and phase stability of the normal spinel structure. *Crystal Growth & Design* **2020**, *20*, 2014–2018.

(36) Speight, J. G. *Lange's handbook of chemistry*; McGraw-Hill Education, 2017.

(37) Song, J.; Shin, D. W.; Lu, Y.; Amos, C. D.; Manthiram, A.; Goodenough, J. B. Role of Oxygen Vacancies on the Performance of $Li[Ni_{0.5-x}Mn_{1.5+x}]O_4$ (x= 0, 0.05, and 0.08) Spinel Cathodes for Lithium-Ion Batteries. *Chemistry of Materials* **2012**, *24*, 3101–3109.

(38) Coelho, A. A. TOPAS and TOPAS-Academic: an optimization program integrating computer algebra and crystallographic objects written in C++. *Journal of Applied Crystallography* **2018**, *51*, 210–218.

(39) Leineweber, A.; Mittemeijer, E. J. Anisotropic microstrain broadening due to compositional inhomogeneities and its parametrisation. *Zeitschrift fur Kristallographie, Supplement* **2006**, *1*, 117–122.

(40) Leineweber, A. Description of anisotropically microstrain-broadened line profiles by Edgeworth series. *Zeitschrift fur Kristallographie* **2009**, *224*, 432–445.

(41) Leineweber, A. Composition-induced microstrain broadening: From pattern decomposition to whole powder pattern modelling procedures. *Materials Science Forum* **2010**, *651*, 131–153.

Graphical TOC Entry

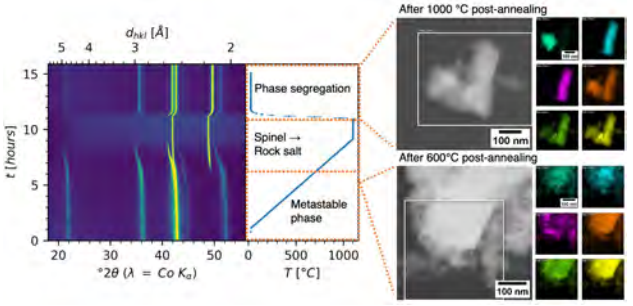

For Table of Contents Only